Demonstration and Analysis of Conditions to Obtain a High Strength Inconel 625 to Stainless Steel 304L Interface by Directed Energy Deposition

A.J. STAIR, BRYAN A. WEBLER, JACK L. BEUTH, and MAARTEN P. DE BOER

Functional grading (FG) is often used to bond dissimilar metals. However, that approach is complicated from a manufacturing perspective, and the associated challenges can outweigh the benefits of FG. Here, we investigate a directly bonded interface by transitioning from stainless steel 304L (SS304L) to Inconel 625 (IN625) using powder-feed directed energy deposition with a laser beam energy source (DED-LB). Both cracking and the presence of carbide phases have been reported in this multi-materials system. Conditions that unambiguously achieve crack-free joints have not yet been established. With DED-LB, we consistently observe solidification cracking in melt pools containing > 50 wt pct SS304L, while no cracking is observed in melt pools with < 40 wt pct SS304L. Variations on the most up-to-date solidification cracking model are applied to gain insight into the cracking dependencies. Parameters that give rise to defect-free single layers also enable defect-free multilayer prints despite the additional thermal cycling. Upon printing and testing full-sized ASTM E8 tensile specimens, the interface is sufficiently strong that failure occurs solely within the SS304L region, indicating a joint strength of > 650 MPa. Thus, a simple method to attain high strength joints for these dissimilar metal alloys is demonstrated.

I. INTRODUCTION

DISSIMILAR metals are bonded to each other for use in cutting tools, fuel cells, aerospace components, diesel engines, and solar receivers.[1] In this paper we investigate the bonding of creep- and corrosion-resistant IN625 to lower-cost SS304L, a system that has several possible applications, including nuclear reactors that operate at high temperatures and with high thermal gradients.[2]

Independent of the manufacturing method, the welding of dissimilar metals is complicated by mismatches in the coefficient of thermal expansion (CTE), the thermal conductivity, and the melting temperature.[2,3] To address these issues, bonds with gradual compositional gradients, called functionally graded materials (FGMs), are often used. One manufacturing method of interest to create FGMs is powder-feed directed energy deposition with a laser beam energy source (DED-LB), in which metal powders of two different alloys can be mixed with varying ratios as deposition proceeds. However, bonds manufactured by this method can still develop intermetallic phases, which are subject to cracking and other macroscopic defects such as delamination of printed layers.[4–11] If there are specific deleterious compositions, FGMs will be susceptible to the associated defects.[8–11] Such a region of deleterious composition is carefully analyzed by Carroll et al.[11] using electron dispersive spectroscopy mapping, X-ray diffraction, and thermodynamic calculations. They attribute the crack formation to NbC and MoC monocarbide formation. Hence, metallurgical factors can outweigh the benefits of FGM.

In principle, regions with deleterious compositions can be avoided using a direct bonding (DB) method. In direct bonding, the composition is controlled through the dilution of the base alloy in the melt pool. Compositional "jumps" between layers can be created. Studies focused on bonding austenitic stainless steels to Inconel alloys, either by creating FGMs[11–14] or by using direct bonding,[15] are listed in Table I. In each paper, three-dimensional structures are fabricated. Only the study of Carroll et al.,[11] which joins SS304L to IN625, reports cracking within the transition region between alloys.

A.J. STAIR, JACK L. BEUTH, and MAARTEN P. DE BOER are with the Department of Mechanical Engineering, Carnegie Mellon University, 5000 Forbes Ave, Pittsburgh, PA 15213. Contact e-mail: mpdebo@andrew.cmu.edu. BRYAN A. WEBLER is with the Department of Materials Science Engineering, Carnegie Mellon University, 5000 Forbes Ave, Pittsburgh, PA 15213

Table I. Stainless Steel to Inconel Bonds Showing the Specific Alloys Used, Methods for Controlling the Composition of the Bonded Region, and Dimensions (L× W× H) of the DED-LB-Manufactured Structure

	Cracking Reported	Steel Type	Inconel Type	Bonding Method	Dimensions (mm)
Carroll[11]	Yes	304L	625	FGM	16 × 16 × 34
Chen[12]	No	316L	625	FGM	~ 5 × 75 × 30
Shah[13]	No	316L	718	FGM	~ 5 × 30 × 30
Zhang[14]	No	316L	625	FGM	10 × 20 × 20*
Feenstra[15]	No	316L	625	DB	15 × 15 × 20
Current Work	Yes	304L	625	DB	23 × 23 × 56

*Indicates structure designed to decrease in length and width as powder composition changes.

Table I implies that deleterious compositions are generally avoided when bonding these materials. However, our previous DED-LB work bonding IN625 to SS304 consistently reveals cracking in single layer beads and pads[16] when SS304L content is greater than 50 wt pct. This discrepancy between other literature and our results gives rise to several important questions.

1. Given the simplicity of direct bonding by DED-LB and the large discrepancy in reported results, can conditions for direct bonding be determined under which cracking reproducibly does and does not occur?
2. In the absence of cracking, how strong is the bond?
3. What are the sources of cracking when it does occur?

To address those questions, this paper is organized as follows. In Section II, we describe Materials and Methods. We choose DED-LB conditions that result in a factor of four increase in deposition rate compared to our previous work.[16] In Section III, Results, we demonstrate conditions under which, reproducibly, cracking occurs or does not occur. Under conditions in which cracks are absent, we fabricate ASTM E8 flat tensile bars and determine a lower bound joint strength of 650 MPa. In Section IV, Discussion, we explore the relative influence of power, scan speed and melt pool composition on cracking susceptibility. We find that the latter is the most important factor, and that the cracks are due to solidification cracking. We then apply the models of Kou[17–22] to evaluate their success in predicting cracking. We draw conclusions in Section V.

II. MATERIALS AND METHODS

In all experiments we deposit Inconel 625 powder on SS304L build plates with varying DED-LB process parameters. Spherical Inconel 625 powder with a diameter size range from 53 to 90 μm is supplied by Matexcel. The build plates are supplied by Rolled Alloys as hot-rolled, annealed, and pickled (HRAP) SS304L stainless steel plate. The compositions for the powder and plates are shown in Table II.

Fabrication is done using a Trumpf TruLaser Cell 3000 DED-LB system, equipped with a TruDisk 6001 laser and a 3 Beam SO 12 Nozzle. Depositions are performed in an enclosed, non-inert environment under ambient temperature. A 3-axis gantry system moves the nozzle, which contains the laser lens and powder outlets. The TruDisk wavelength is 1030 nm and its maximum power is 6 kW. We set the adjustable laser focal diameter to 3 mm in all experiments. The SO 12 nozzle maximum power is 3 kW and it can feed powder in the approximate size range of 45–90 μm. An argon gas stream flowing at 6 L/min carries powder from hoppers, and additional argon shielding gas flowing at a rate of 10 L/min is directed at the molten melt pool from the nozzle. The powder flow rate, in g/min, for each experiment is measured by collecting and weighing powder that flows through the nozzle over a 2.5 minute period.

The determination of machine parameter settings is a key step for building three-dimensional structures, and hence is detailed here. Single tracks are straight deposition passes along a length sufficient for a melt pool to form and reach steady state. In this work, the length of single tracks is 20 mm. The laser power and scan speed are varied to measure the effect of parameters on the wt pct SS304L in the melt pool. We deposit three parallel single tracks at each parameter set, with a 6 mm center-to-center spacing between each track. We deposit only one track per parameter set at a time, moving on to the next set at a different build plate location. After one track at every parameter set is deposited, a second set of tracks is deposited, and so on. Depositing one track at a time prevents local heat buildup in the build plate. Several single track experiments are conducted using powder flow rates (*PFRs*) ranging from 2 to 18 g/min. The laser parameters of two of the tests, at 10 and 18 g/min, are shown in Table III.

The cross-sectional areas of the melt pool, measured above and below the surface of the build plate, are A_a and A_s, respectively. The ratio of the areas approximates the wt pct SS304L because SS304L and IN625 have very similar densities. The wt pct SS304L is found as

$$\text{wt pct SS304L} = 100\,\text{pct} \times A_S/(A_S + A_a) \qquad [1]$$

Previous work by Jones *et al.* shows that for single tracks the measured wt pct of major alloying elements matches well with the expected values based on

Table II.   Elemental Wt Pct Composition for IN625 Powder and SS304L Build Plate

	Fe	Cr	Ni	Mo	Mn	Si	C	Nb	Cu	Al	Co	N	Ti	P	S
IN625	2.2	22.0	Bal	8.93	0.015	0.25	0.013	3.73	0.061	0.071	0.013		0.039	< 0.005	< 0.003
SS304L	bal	18.2	8.09	0.430	1.78	0.306	0.0233		0.490		0.269	0.0911		0.0310	0.0010

Table III.   Range of Laser Powers and Velocities and Increments Used for Initial Single Tracks and Single Layers, Printed in a 4× 4 Grid

	Power (W)	Velocity (mm/min)
Range	1200–2100	900–2700
Increment	300	600
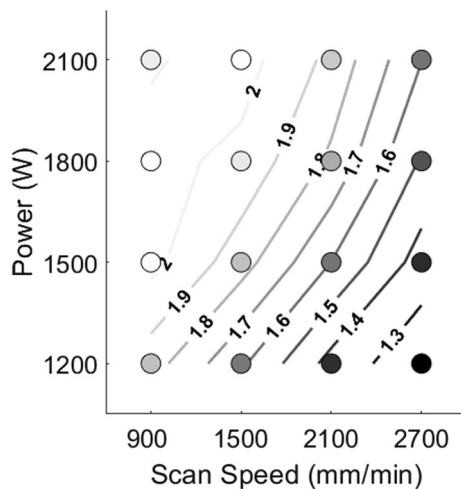
Fig. 1—Hatch spacing in mm used for initial single layer tests with a powder flow rate of 10 g/min.

dilution.[16] All further calculations of compositions use this equation unless otherwise specified.

Single layers are multiple overlapping single tracks with the centers of the tracks offset by the hatch spacing, HS. It is calculated using measurements from the previous single track experiment. Accordingly,

$$HS = A_a/h_{max} \qquad [2]$$

Here, h_{max} is maximum height above the build plate. A Keyence optical profilometer (VR-5000 Series Wide Area 3D Measurement System) measures h_{max} and A_a. This is a simplified version of the equation from Zhang et al.[23] The G-code controlling the machine toolpath in our experiments is generated by hand. Eq. [2] gives the largest hatch spacing that theoretically can be printed while maintaining low lack of fusion porosity. By using this HS, our aim is to create relatively smooth printed layers while avoiding excess material buildup where beads overlap. Hatch spacings determined for the PFR = 10 g/min experiment are shown in Figure 1. The hatch spacing increases with laser power but

decreases as the laser scan speed increases. The single layers in this work are 20 × 20 mm, with additional "contour" tracks deposited perpendicularly across the ends of the previous tracks to provide a smoother edge. All beads are printed consecutively in the single layer experiment. Instead of moving between locations with different parameters at each to reduce heat buildup, we implement an inter-track wait time of 3 seconds between each track in the layer.

Multilayers are two or more single layers deposited on top of each other. The purpose of the multilayers is to determine the effect of thermal cycling in the interface layer caused by the heat affected zones (HAZ) of subsequent layers before printing a full-sized tensile specimen. The designed multilayer dimensions are approximately 17 × 17 × 15 mm. We deposit multilayers using three sets of crack-free parameters found from single layer experiments, as shown in Table IV. Each parameter set is labeled by the wt pct SS304L in the first layer. The designed layer height for each multilayer is the height of the corresponding single layer, as measured by the optical profilometer. Each layer of a multilayer is rotated 90° from the previous, so the tracks are perpendicular to the previous layers. Less heat is conducted from melt pools printed atop parts with small cross-sections than from melt pools printed directly on the build plate. To compensate we increase the inter-track wait time to 6 seconds. Additionally, the multilayers are each printed one layer at a time to prevent heat buildup between layers. One multilayer cools for the duration it takes to travel to and print the other two. We also separate the multilayers spatially from each other to prevent excessive heat from accumulating locally. Two multilayers are located 30 mm apart on the same build plate, with the third on a separate build plate. This means that for every set of layers printed, each build plate cools for at least one inter-layer wait time. We also deposit multilayers at a higher stainless steel content of 66 wt pct, which is intentionally meant to induce cracking in the first layer. Parameters are shown in the last column of Table IV.

The tensile specimen build is a tall multilayer of 23 × 23 × 56 mm. It is fabricated on the edge of a 25 mm thick SS304L build plate. The Inconel portion of the structure is taller than any structure from the studies in Table I, and the print volume is about seven times that of the 17 × 17 × 15 mm structures. The print parameters are shown in Table V. We make some adjustments from the multilayer printed at 1500 W based on the previous experimental results. Since there is only one multilayer in this experiment, the inter-layer wait time is shortened to 120 seconds. The hatch spacing is also reduced by a small amount to eliminate a minor

lack of fusion porosity in the first layer of a multilayer build. Layer height is increased to compensate for overbuilding of the previous prints. The specimens are cut from the build and plate by wire electrodischarge machining (wire EDM). Two flat specimens, 6 mm by 5 mm in the gage section, are cut side-by-side, as outlined in Figure 2. Each specimen outline is cut three specimens deep for a total of six. Tensile testing is performed using an Instron Model 4469 tensile frame. The strain rate for testing is 0.1 mm/s. An extensometer is used to measure strain during the experiment. The extensometer is placed in the center of the gage section and measures approximately equal spans of SS304L and IN625.

The dimensions above the build plate for the single track, single layer, and multilayer experiments are measured using the optical profilometer. In addition to a single layer print, multilayers with 2, 5, and 10 layers are printed for 66 wt pct SS304L to determine the effect the additional layers would have on cracks in the first layer.

The plates are then sectioned to create samples. There are three single tracks at any given parameter setting. There is only one single layer and one multilayer structure per sample. The samples are cross-sectioned perpendicular to the laser travel direction for single tracks and single layers, and to the base layer of the multilayers. The cuts are made near the center of each. The metal samples are then mounted and polished. The final polishing uses a 0.05 μm colloidal silica solution.

After polishing, the single track, single layer, and multilayer cross-sections are analyzed optically using the Zeiss Axio Imager Z2 Vario. The area of the single tracks both above and below the surface of the build plate are measured using a combination of the built-in software and the ImageJ software. The single layers are examined for any evidence of cracking. Multilayer images are processed in the ImageJ software to measure the porosity of the sample. Greyscale microscope images are loaded, and then converted to black and white, so that the pores in the sample appear black against a white background of the metal. Only the region above the build plate is selected for porosity measurement. The percentage of area containing black pixels is the porosity of the fabricated structure. Micrograph density results for specimens with very low porosity have been shown to be similar to results using the Archimedes method on the same samples.[24]

An FEI Quanta 600 FEG scanning electron microscope is used to analyze the microstructure and composition of single layers, multilayers, and excess material cut from the tensile specimens.

III. RESULTS

A. *Single Tracks*

Figure 3 shows a contour map of the SS304L content at each parameter setting of the $PFR = 10$ g/min single track experiment. There is an increase in steel content with laser power at every scan speed. At the lower powers, the contours are nearly horizontal, indicating little dependence on scan speed.

Upon closer inspection, many single tracks and single layers in Figure 3 melt pool compositions reveal cracking. To decrease the wt pct SS304L, a second single track experiment with the previous parameters at $PFR = 18$ g/min is conducted. Figure 4 shows the wt pct SS304L versus laser power at a scan speed of 900 mm/min for the two PFR s. It can be seen that for same parameters, the stainless steel content of the 18 g/min tracks is more than 30 pct lower than that of the 10 g/min tracks.

B. *Single Layers*

Single layers are more likely to exhibit cracking than single tracks. This is due to the greater number of tracks as well as the reheating from multiple passes. Figure 4 also shows cross-section images of single tracks and single layers printed at 900 mm/min and 1500 W for powder flow rates of 10 and 18 g/min. The single layer with the higher SS304L content contains a significant amount of cracking. There is a large crack at the top center of each track, which is the last liquid to solidify, along with scattered smaller cracks near the boundary of the beads and build plate. There is no evidence of macro scale cracking in the single layer with a lower stainless steel content.

C. *Multi-Layers*

The deposition of additional layers induces further thermal cycling in the initial layer. In multi-pass welding of stainless steels to Inconels, additional precipitate formation in reheated regions is reported.[25,26] Although Jones *et al.* deposited only single layers, they performed a heat treatment and showed that crack-free single layers did not develop cracks during subsequent heat treatment.[16] Figure 5 shows the first few layers of the multilayers deposited with $PFR = 18$ g/min The calculated wt pct SS304L of the nth layer, $(wt.pct(Layer1))^n$, is on the right.

The porosity of the crack-free multilayers, Figure 5, is measured to determine which parameter set to use for the tensile specimens. There are different types of porosity depending on the process parameters. Interlayer porosity is often caused by low global energy density,[27] which in this case is controlled by the laser power as all other parameters have been kept constant across the blocks. Interlayer porosity is also characterized by elongated or irregular pores caused by lack of fusion (LOF).[27,28] These descriptions strongly resemble the 1200 W multilayer in Figure 5(c). The shape and location of the pores, coupled with the lower laser power, indicate that the increased porosity in this sample is likely due to LOF. Most pores are not elongated in the higher power multilayers. The pores occur much more randomly than in the 1200 W multilayer, especially in the higher layers of the image. Higher global energy density, caused by higher power, is associated with gas entrapment porosity.[27] The

Table IV. Print Parameters for Multilayer Prints, Labeled by the Nominal Composition of the First Layer

	20 Wt Pct SS304L	30 Wt Pct SS304L	40 Wt Pct SS304L	66 Wt Pct SS304L*
Laser Power	1200 W	1500 W	1800 W	2100 W
Laser Scan Speed	900 mm/min	900 mm/min	900 mm/min	900 mm/min
Powder Feed Rate	18 g/min	18 g/min	18 g/min	5.0 g/min
Hatch Spacing	1.75 mm	1.89 mm	1.99 mm	1.9 mm
Layer Height	0.853 mm	0.850 mm	0.846 mm	0.250 mm
Inter-pass Wait	6 s	6 s	6 s	6 s
Inter-layer Wait	154 s	160 s	160 s	120 s

*Prints at this composition are designed to crack in the first layer, and were printed to be 17 × 17 × 3 mm

Table V. Print Parameters for the IN625 Portion of the Bimetallic Tensile Specimen

|	30 Wt Pct SS304L
Laser Power	1500 W
Laser Scan Speed	900 mm/min
Powder Feed Rate	18 g/min
Hatch Spacing	1.80 mm
Layer Height	0.930 mm
Inter-pass Wait	6 s
Inter-layer Wait	120 s

Fig. 2—IN625 tensile specimen column and SS304L build plate with the tensile specimens outlined.

measured density of our prints is consistent with other IN625 experiments, which measured densities of 99–100 pct using the Archimedes method.[29–31] The 1500 W laser power is chosen for the final build because it has the highest density.

Figure 6(a) shows a single layer with 66 wt pct SS304L. It contains a small crack near its base, as indicated by the arrow. Figures 6(b) through (d) show multilayers printed for the same parameters with 2, 5, and 10 layers respectively. The cracks become larger as the number of layers printed increases. The height of each individual layer is ~ 0.25 mm, and the larger crack in the 10 layer build is roughly 2 mm long extending into the fifth layer of the build. This shows that, rather than being remelted, cracks at the top of a layer can continue to propagate through the additional layers.

D. Tensile Properties

Stress-strain curves from three bimetallic and three SS304L build-plate specimens are shown in Figure 7, along with images of the fractured specimens. The average values from the experiments and the vendor-provided specifications for the SS304L plate are summarized in Table VI. Our measured ultimate tensile strength for the build plate is slightly above the vendor specifications. The yield strength, defined as the 0.2 pct offset, and the elongation at fracture, agree within 3 pct of the vendor value. The bimetallic specimens fracture in the SS304L region. Their UTS is 3 pct larger than the 100 pct SS304L specimens. The elongation at fracture is lower for the bimetallic specimens, because the IN625 deformation is negligible. This indicates that the interface printed with 30 wt pct SS304L is stronger than the base plate, and provides good evidence that by avoiding cracking a strong joint is fabricated.

Experiments in both IN625 and SS304 show that columnar grains grow away from the build plate in DED-LB.[29,32,33] They grow at an angle between 60 and 90° from the build plate in some IN625 studies.[34,35] The grain orientation causes anisotropic properties, and the yield strength is lowest along the build direction, perpendicular to the build plate. Our printing method, depositing IN625 on top of the SS304L build plate, results in the tensile axis being located along the build direction. Hence, the joint strength of 650 MPa is a lower bound.

The extensometer for the bimetallic specimens spans roughly half of the IN625 and half of the SS304L. The plastic strain is primarily in the SS304L. The bimetallic yield strength of 338 MPa using the 0.2 pct rule is somewhat higher than the 295 MPa of SS304L because
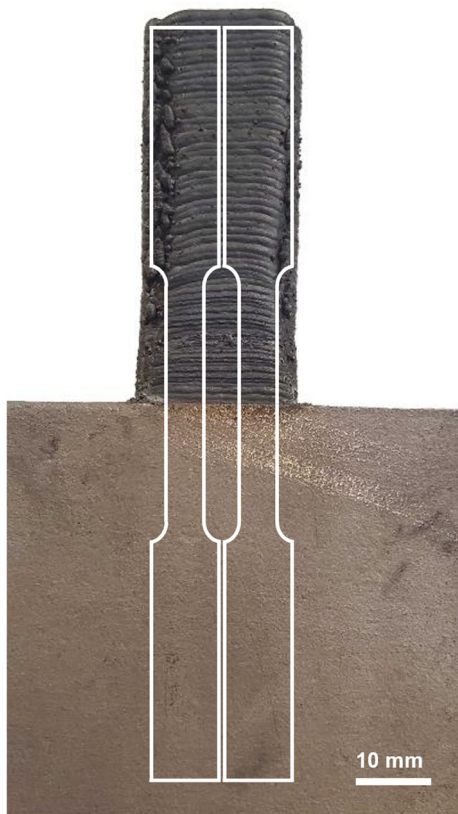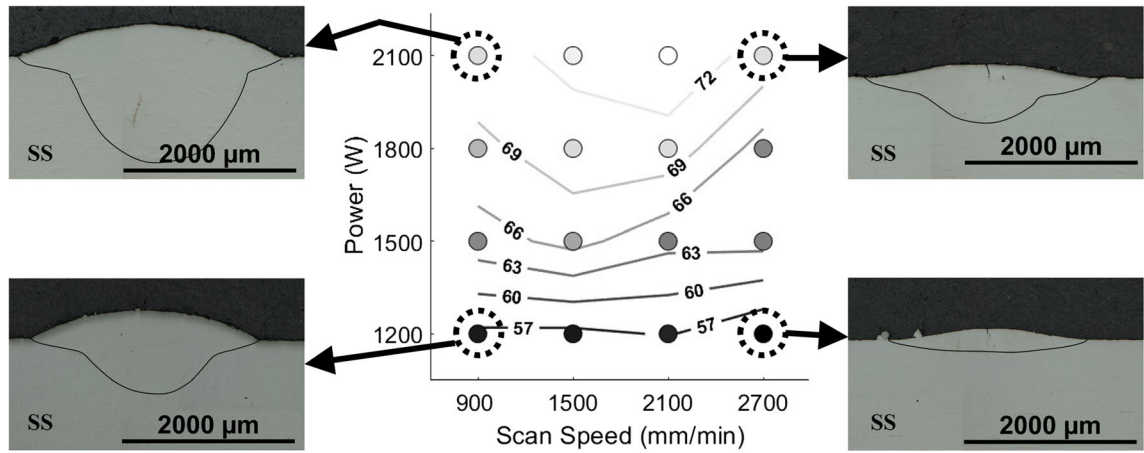
Fig. 3—Change in SS304L content with power and scan speed parameters for a single-track experiment with PFR = 10 g/min. Contours are wt pct SS304L.
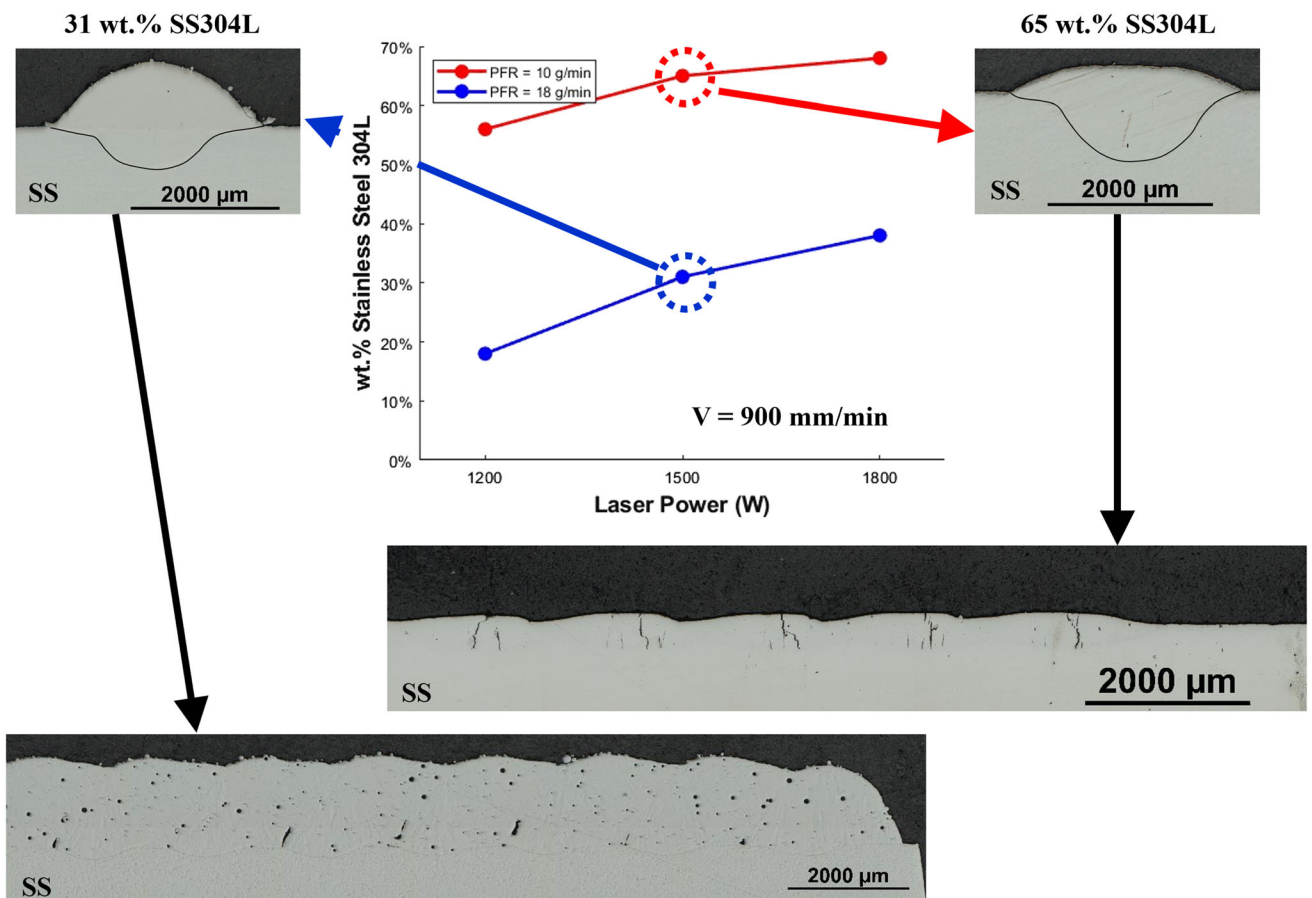

Fig. 4—A plot showing dilution of SS304L versus laser power at a scan speed of 900 mm/min for two different powder flow rates. Optical images of single tracks and single layers at 1500 W are also shown.

it equates with a larger nominal strain in the SS304L portion. The IN625 portion of the gage section has a uniform thickness, and the necking only begins in the SS region away from the interface.

EDS line scans taken along the tensile axis from the printed tensile specimen block are shown in Figure 8. The measured Fe and Ni composition are shown in blue and orange, respectively. Figure 8 also shows the nominal compositions calculated from the single-track experiments, with Fe in red and Ni in green. Previous work has shown that the interface for this system is ~ 20 μm in length,[16] which is negligible compared to the layer height of our print. For this reason, the interface in Figure 8 is simply shown as a vertical line between the
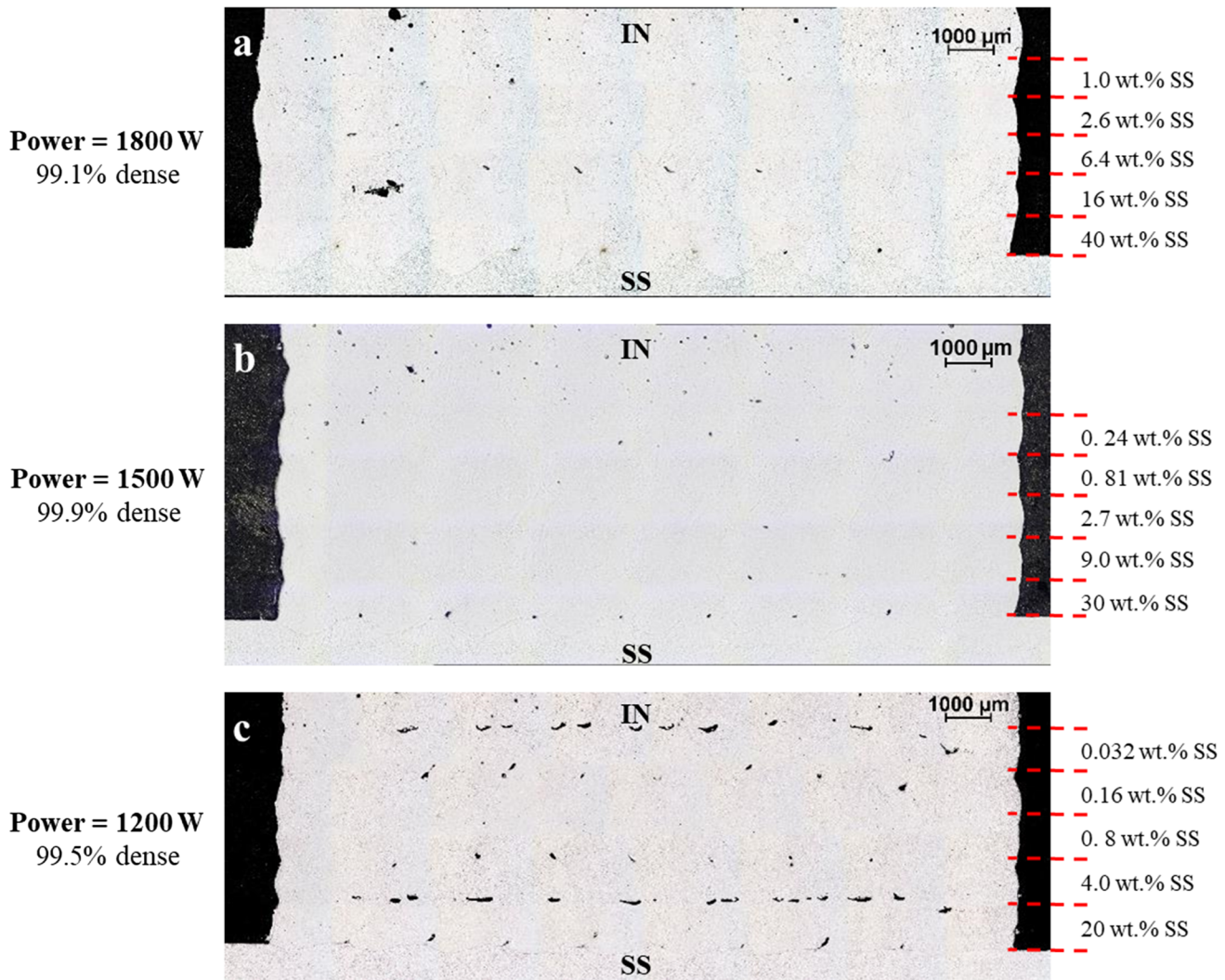
Fig. 5—Multilayer cross-sections with first layer nominal compositions of (*a*) 40 wt pct, (*b*) 30 wt pct, and (*c*) 20 wt pct SS304L. Here *PFR* = 18 g/min.
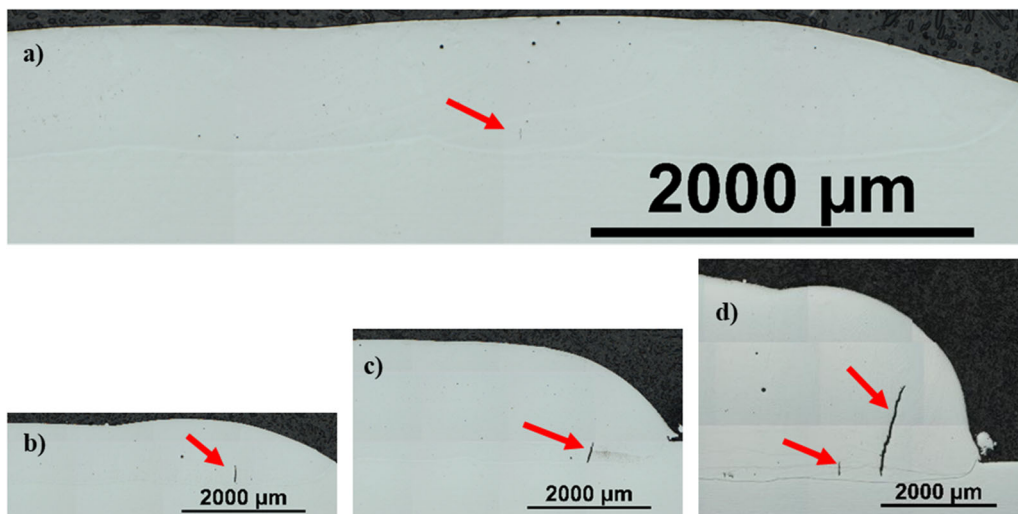
Fig. 6—Optical microscope images of interfaces with 66 pct SS304L in the first layer. (*a*) a single layer print, (*b*) a 2-layer print, (*c*) a 5-layer print, and (*d*) a 10-layer print. Each show crack(s) of increasing size as more layers are printed, as indicated by red arrows (Color figure online).
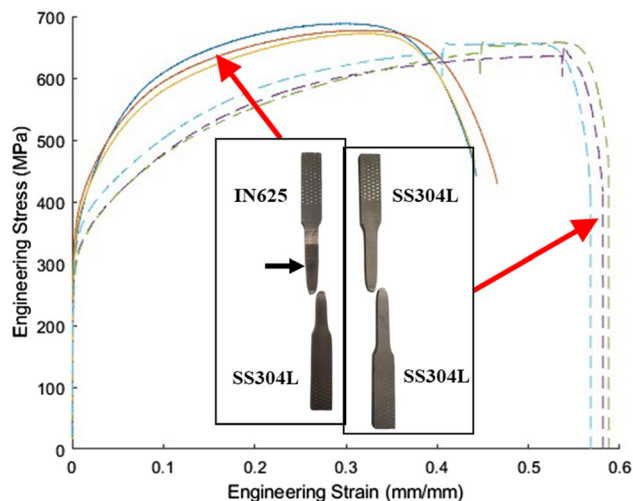
Fig. 7—Engineering stress-strain curves for bi-metallic tensile specimens (solid lines) and SS304L baseplate specimens (dashed lines) with images of the respective specimens (black arrow indicates the interface) (Color figure online).

base plate and Layer 1, where we see a sharp decrease in Fe content. The length of the layers along the x-axis is the layer height given in Table V.

The composition of our full build varies more than reported in single tracks.[16] The Layer 1 composition of the tensile specimen is not uniform, as there is higher stainless steel content near the bottom of the layer. The average composition of the first layer is 27 pct SS304L, which is somewhat lower than the single track composition of 30 pct for the same parameters, as circled by dashed blue in Figure 4. In comparison, the composition of Layer 2 at 8.6 pct SS304L agrees better with the prediction of 9 pct shown in Figure 5(b). The discrepancy in Layer 1 can be explained by the fact that Eq. 1 applies to isolated single tracks. In a layer, each single track remelts an overlapping edge of the track next to it because the hatch spacing is less than the melt pool width. This remelted portion contains less SS304L than the substrate, and hence the resulting SS304 content in the layer is somewhat lower than assumed. This discrepancy should decrease in the higher layers since progressively less SS304L is assumed in them.

IV. DISCUSSION

A. Single Layers

Figure 9 plots the linear energy density versus wt pct SS304L of all our single track and single layer experiments. Linear energy density (J/mm) is a measure of heat input found by dividing the laser power by the scan speed of the laser. Single tracks and single layers with no macro scale cracks observed under an optical microscope are represented by a blue " + " and a blue "■", respectively. Single tracks and single layers with cracks are represented by a red "x" and a red "♦", respectively. The vertical dashed line delineates an approximate boundary between melt pool compositions where

cracking does or does not occur. Based on the plot, there is a strong dependence on SS304 content and little to no dependence on linear energy density, indicating that composition is the driving factor for cracking in this system.

While composition influences intermetallic presence, the cooling rate plays a role as well. We would expect to see more large intermetallic precipitates at lower cooling rates, which corresponds to higher linear energy densities.[36] There are both uncracked and cracked samples in a narrow composition band from 55 to 60 pct SS304L. Samples printed with higher energy densities in this range contained less cracking, the opposite of what we would expect if cracking were based on intermetallic precipitate growth driven by cooling rates. The lack of correlation between linear energy density and cracking suggests that the cracking is not caused by solid-state precipitation of intermetallics.

Figures 10(a) and (b) show backscatter SEM images at two magnifications, respectively, of a cracked portion of a single layer with 56 wt pct SS304L. The single layer with this composition reveals a cellular solidification microstructure. Grains with different cell orientations are seen by comparing the top right versus the left-hand portion of Figure 10(b). Additionally, microsegregation of elements can be seen in Figure 10(b). The segregants are the last material to solidify between the two grains. Figures 10(c) through (d) show EDS maps of Mo and Nb in the same region as 10b. They show a much higher concentration of these elements in the segregated liquid. The cracks observed occur along these grain boundaries, indicating intergranular solidification cracking. There is a portion of segregated material, indicated by a white arrow, where the liquid is only partially filled in. This further indicates that the cracking in the single layer is due to molten metal that is unable to fill a channel between the solidifying grains as they shrink.

Traditional manufacturing of IN625 and gas tungsten arc welding have shown a combination of both NbC and Nb and Mo rich Laves phases.[37] The solidification trends have shown that increasing the ratio of C to Nb increases the likelihood of NbC precipitate formation.[37] This would indicate less Laves phase and more NbC precipitate formation at higher concentrations of SS304L. However, higher amounts of Fe present in Alloy 718 have been shown to increase the formation of Laves phase,[37] which would suggest the formation of Laves phase in mixtures with high SS304L content. It should be noted that there is a large amount of uncertainty in identifying the amount and type of secondary phases based on composition alone, since many secondary phases are composed of the same alloying elements with overlapping ranges of composition for each element.

In traditional manufacturing, solution annealing at high temperatures can eliminate Laves phase.[37] However, previous work has shown that high temperature heat treatments on samples with solidification cracking leads to crack growth, while there is no crack formation during heat treatment for compositions without cracks.[16] Nonetheless, post-print solution annealing of crack-free samples may dissolve Laves phase and

Table VI. Manufacturer Mechanical Property Measurements for SS304L Plate Compared to Our Measured Data for SS304L and Bi-metallic Specimens

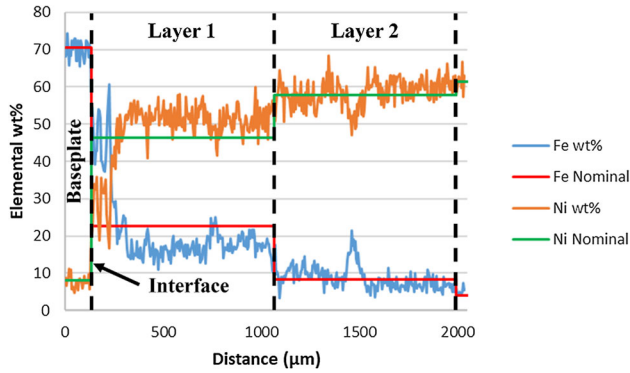| Property	UTS (MPa)	Yield Strength (MPa)	Elongation (pct)
SS304L Vendor Val	609	285	56
SS304L Measured	656	295	58
Bi-metallic	679	338	45

Fig. 8—EDS line scan of the first two layers of printed material in the bimetallic tensile specimen. Measure values of Fe (blue) and Ni (orange) are shown alongside the nominal values of Fe (red) and Ni (green) (Color figure online).
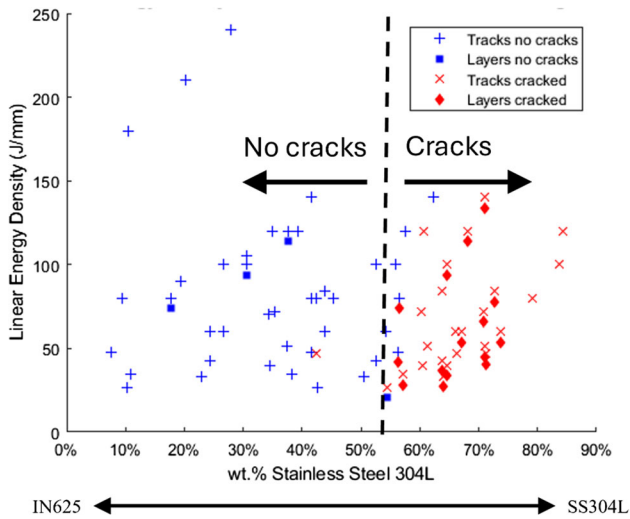
Fig. 9—Plot of linear energy density vs. wt pct SS304L showing the presence of macro-scale cracks in single bead and single layer experiments observed using optical microscopy. The dashed vertical line indicates the lowest content of SS304L at which cracking is consistently observed.

serve to inhibit crack nucleation in bimetallic prints, thereby improving service life.

B. Solidification Cracking Analysis

The observed liquid feeding leads us to apply Kou's solidification cracking criterion[17] in an attempt to explain the observed cracking. It is developed according to the idea that narrower channels of high aspect ratio

are more susceptible to cracking than wider channels.[17] The Kou criterion then states that the slope of temperature versus the square root of the fraction solid, $(f_{SB})^{1/2}$, can indicate whether the liquid channel between two solidifying grains will have a high aspect ratio, and therefore be difficult to feed.[17] A larger absolute value of slope on the graph of T vs. $(f_{SB})^{1/2}$ corresponds to a higher aspect ratio liquid channel. The slope used is the maximum slope within a certain solidification range. For an alloy with a vulnerable solidification region of $0.90 < f_{SB} < 0.99$, as used in Kou,[17] the maximum slope would be taken in the range $0.95 < (f_{SB})^{1/2} < 0.995$.[17] This method is used to compare the relative cracking susceptibility of several alloys.[17] We apply the Kou cracking criterion to several compositions of our gradient and compare the results to our experimental data.

Kou's original work uses the Scheil solidification model in Pandat[38] to compare Al casting alloys.[17] Later work by Kou and coworkers with this method is published for different Al[18] and Inconel alloys.[19] Soysal's study with several carbon steels compares the results of the Kou criterion when using a classic Scheil solidification model, a Scheil solidification with back diffusion model, and an equilibrium solidification model.[20] Soysal finds that the most reasonable solidification model to use when applying the Kou criterion is the Scheil with back diffusion model.[20] Soysal et al. apply this criterion to different stainless steels.[21]

We repeat the modeling of Soysal[21] using Scheil solidification with back diffusion in Thermo-Calc (TC) 2021b.[39] The thermodynamic and mobility databases used were TCFE11 and MOBFE6 for Fe-based mixtures, and TCNI11 and MOBNI5 for Ni-based mixtures.[39] Carbon and nitrogen are labeled as fast diffusers in calculations. The cooling rate is taken to be 420 K/s, while the remaining settings are left as default values.[21] The maximum slope of the solidification curve is taken both in ranges $0.8 < (f_{SB})^{1/2} < 0.99$ and $0.8 < (f_{SB})^{1/2} < 0.995$ and the order of susceptibility is compared to experimental data. It is found that a maximum $(f_{SB})^{1/2} = 0.99$ should be taken for all but SS310, which should have a maximum $(f_{SB})^{1/2} = 0.995$.[21] We attempt to recreate the TC results using the same version of the software, compositions, and settings given in the paper.[21] However, as is shown in Figure 11, while we can generally match the susceptibility trend, our slopes are somewhat higher than those reported in Soysal's paper.[21] We choose to apply the criterion to compositions containing a mixture of SS304L and IN625, as the order of the slopes is emphasized above the exact values in the papers.[17–21]
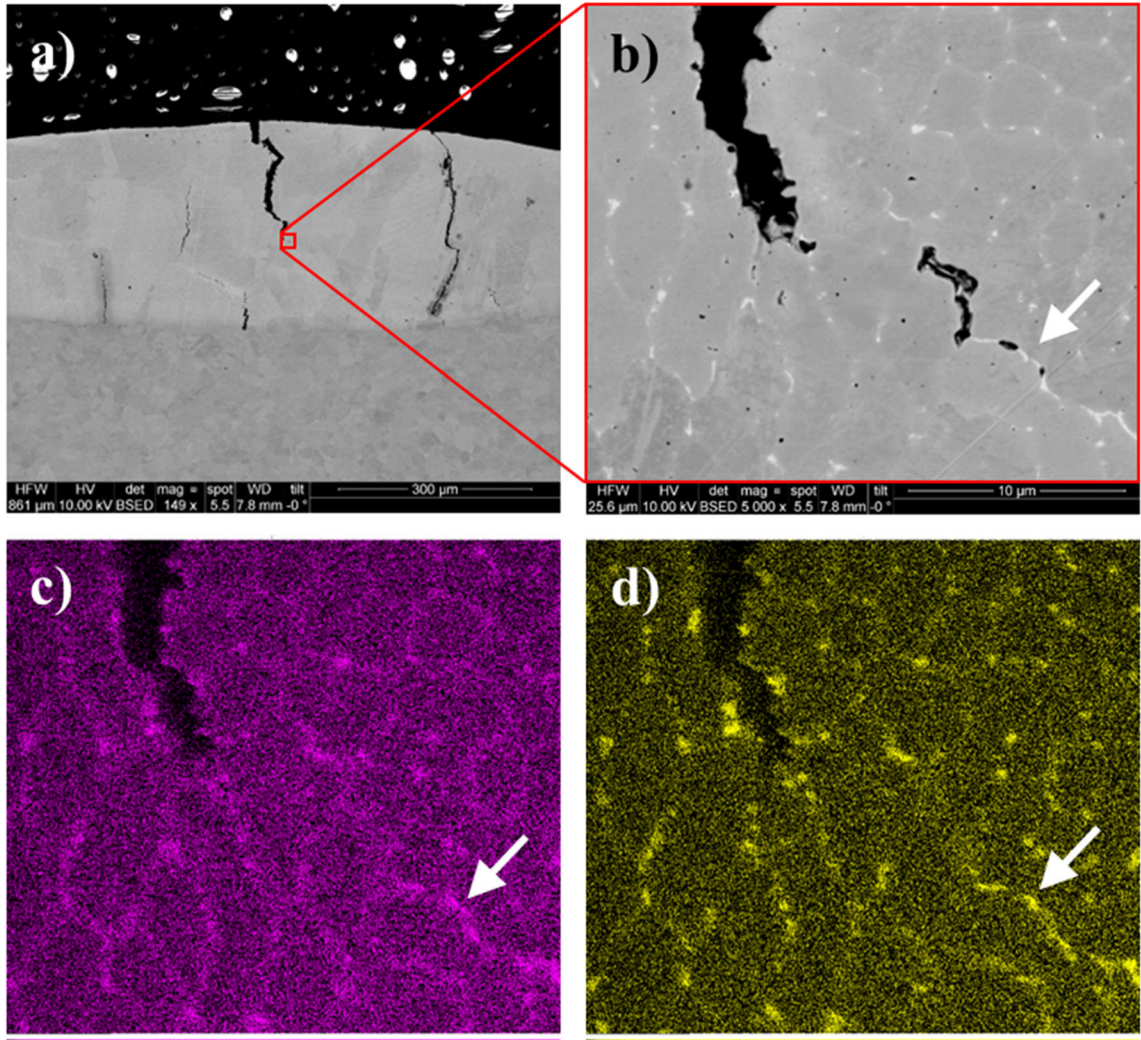
Fig. 10—(*a*) SEM image of a single layer experiment with significant cracking, (*b*) magnified image of the tip of a crack showing evidence of segregants at grain boundaries and at the crack tip as indicated by an arrow, (*c*) Mo EDS map and (*d*) Nb EDS map showing increased amounts of these elements as segregants at the grain boundaries and crack tips.
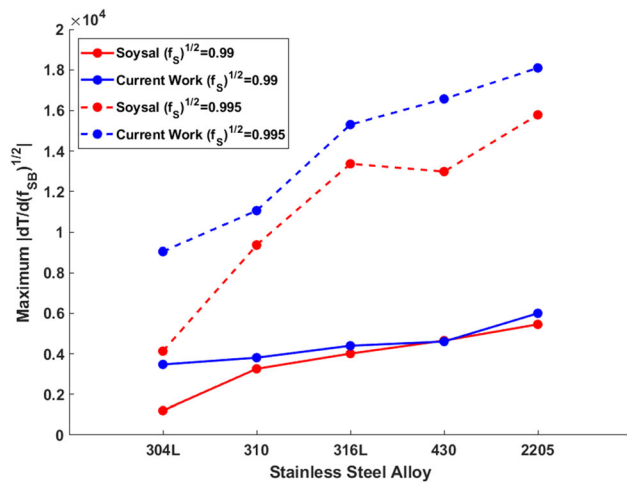

Fig. 11—Plot of maximum $|dT/d(f_{SB})^{1/2}|$ for stainless steels using data from Soysal and Erk[21] (red) and values calculated in the current work (blue) (Color figure online).
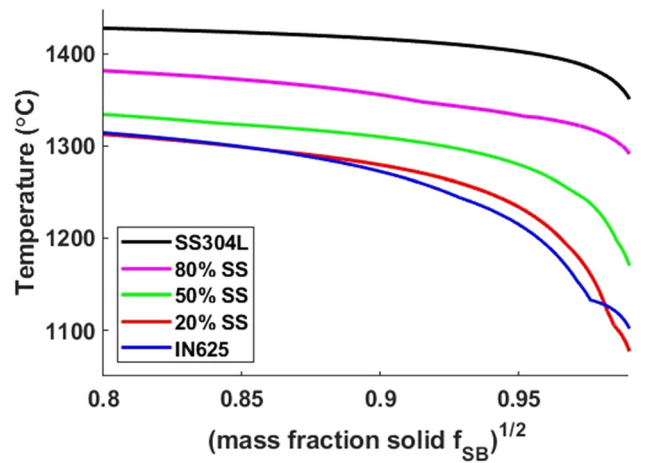
Fig. 12—T vs. $(f_{SB})^{1/2}$ curves for key compositions in the IN625-SS304L system.
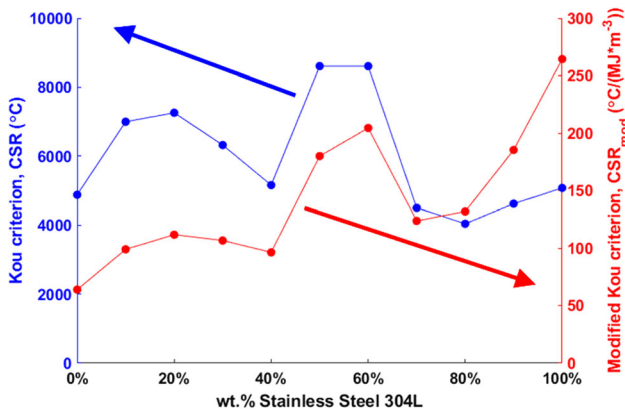
Fig. 13—Maximum steepness of the T vs. $(f_{SB})^{1/2}$ for the Kou criterion on the left axis and for the Modified Kou criterion on the right axis, each vs. wt pct SS304L.

We evaluate the compositions from IN625 to SS304L in increments of 10 wt pct SS304L, based on the compositions given in Table II. The temperature step for evaluation in Thermo-Calc is $\Delta T = 1$ K, and the cooling rate is 1500 K/s. The slope is plotted from $0.8 < (f_{SB})^{1/2} < 0.99$ when the wt pct SS304L is 50–100 pct since there is then more Fe than Ni. This range is used for most stainless steels in previous work.[21] However, papers using Ni alloys employ an upper limit of $(f_{SB})^{1/2} = 0.98$,[19] so we use that value for the remaining compositions, which contain more Ni than Fe. The maximum slope in the given ranges is the crack susceptibility ranking, CSR. We determine the slope at $(f_{SB})_i^{1/2}$ using a backward difference. Accordingly,

$$CSR = \max\left(\frac{|dT|}{d(f_{SB})^{\frac{1}{2}}} = \frac{|T_i - T_{i-1}|}{(f_{SB})_i^{\frac{1}{2}} - (f_{SB})_{i-1}^{\frac{1}{2}}}\right) \quad [3]$$

A plot of T versus $(f_{SB})^{1/2}$ for IN625, 20 pct SS304L, 50 pct SS304L, 80 pct SS304L, and SS304L is shown in Figure 12. Among the compositions present, the 50 pct SS304L curve reveals the steepest maximum slope while the 80 pct SS304L curve the shallowest absolute value of the maximum slope. Figure 13 shows the numerical values for maximum slope in blue plotted on the left y-axis.

Tang *et al.* modify the Kou criterion by taking the average slope of the T versus $(f_{SB})^{1/2}$ in the range of $0.9 < (f_{SB})^{1/2} < 0.99$ for Al and stainless steels and $0.9 < (f_{SB})^{1/2} < 0.98$ for nickel superalloys.[22] They then divide Eq. [3] by the high temperature toughness, $E_{toughness}$, to take the strength of the material into account. The modified crack susceptibility ranking, CSR_{mod}, is

$$CSR_{mod} = \max\left(\frac{|dT|}{d(f_{SB})^{1/2}} \frac{1}{E_{toughness}}\right) \quad [4]$$

They find this criterion to be more consistent with experimental data from literature and their own Dynamic X-ray Radiography data of Laser Powder Bed Fusion melt pools.[22] We apply the modified Kou criterion, which is called "Index 2" in the Tang paper,[22] to both our previous maximum slope data and the average slope of the solidification curves. The results using the maximum CSR_{mod} slope are shown in Figure 13, as plotted in red on the right y-axis. We use the rule of mixtures as an approximate toughness for the intermediate compositions between the two base metals. High-temperature toughness values were taken from Tang et al.[22] for SS304, and Oliveira et al.[40] for IN625. Using the rule of mixtures is not an accurate approximation of high-temperature toughness. This creates a potential source of error in our crack susceptibility analysis for the modified Kou criterion.

Neither criterion qualitatively agrees well with the data shown in Figure 9. Figure 9 shows there is a low cracking susceptibility, likely increasing gradually with SS304L content, up to 50 pct SS304L. In contrast, Figure 13 shows local peaks at 20 pct SS304L for both cracking susceptibility criteria. Our experimental data also shows that the region of high cracking susceptibility should extend to almost 90 pct SS304L. Figure 13 Kou criterion shows a theoretical susceptibility that is lower from 70 to 90 pct SS304L than from 0 to 40 pct 304L and at 100 pct SS304L. This contradicts our experimental results. All samples with dilutions from 70 to 90 pct SS304L crack, while none of the samples within 0 to 40 pct or 100 pct SS304L show any cracking. The Modified Kou criterion shows a decrease in theoretical susceptibility at 60 pct SS304L, where there are some uncracked samples, and at 70 pct SS304L, at which all the samples are cracked. The Modified Kou criterion also shows the highest theoretical crack susceptibility at 100 pct SS304L, whereas the base alloys should be less susceptible to cracking. Indeed, our experience with SS304L powder on a SS304L baseplate using DED-LB does not reveal cracking. The direct comparison between both criteria and experiments indicates that the criteria are not applicable to intermediate compositions of these dissimilar metals.

C. Further Comparisons to DED-LB Literature

Table I describes whether cracking is observed in DED-LB multilayer structures joining Inconel 625 or 718 to stainless steel 304L or 316L. Table VII summarizes data from DED-LB experiments in which only single tracks or a single layer of IN625 is deposited on a SS304L substrate. Of the reported studies, only one reports cracking. Jones *et al.* report cracks at 61 wt pct SS304L and higher[16] composition at which Jones starts to observe cracking[16] is close to the composition at which cracking is observed in this work. Barragan *et al.* do not report cracking, however the highest stainless steel content in their single tracks is 61 wt pct SSS304L,[41] putting their results in agreement with Jones *et al.*[16] Misra *et al.* also do not report cracking, however their stainless steel content is below 43 wt pct SS304L.[36] This content is below the cracking threshold of both the current work and the previous work by Jones *et al.*[16] Experiments from the previous works [16,36,41] are all conducted at significantly lower laser

Table VII. Literature Process Mapping Experiments Showing the Compositions at Which Cracking Occurred and the Overall Laser Power and Scan Speed Ranges, Along with the Laser Spot Diameter

	Cracking Composition (Wt Pct SS304L)	Crack-free Composition (Wt Pct SS304L)	Power (W)	Scan Speed (mm/min)	Laser Spot Diameter (mm)
Current Work	54–84	8–54	1200–2100	900–2700	3
Jones[16]	61–69	41–61	600–900	900–3600	1.2
Misra[36]	—	20–43	600–1200	600–1000	1.2
Barragan[41]	—	0–61	350	2000	0.8
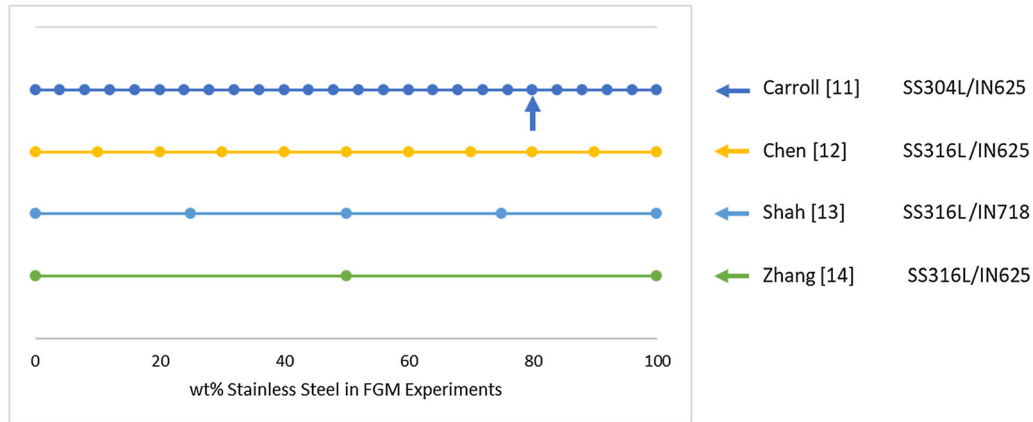
Fig. 14—Weight percent stainless steel in each layer, as represented by dots, of functionally graded structures, with a vertical arrow indicating where cracking is reported. Horizontal arrows on the right indicate that depositions proceed with decreasing SS content.

powers than have been used in the current work, but similar scan speeds. The previous experiments have lower linear energy density, but similar compositions where cracking is observed.[16,36,41] Taken together, these three reports [16,36,41] do not conflict with our assertion that the wt pct SS304L is the primary cause of cracking in the IN625/SS304L system.

Several FGM studies are shown in Figure 14. The experiments deposit Inconel and stainless steel powder mixtures of varying compositions on stainless steel build plates. The nominal composition of each layer in the gradient region is represented by a dot. The wt pct SS in each layer decreases as more layers are printed, as indicated by the leftward-facing arrows next to the plot. Carroll *et al.*,[11] Chen,[12] and Shah[13] each deposited at least one layer with high wt pct SS. Carroll's structure cracked at ~ 80 wt pct SS304L,[11] however Chen and Shah each reported no cracking despite having layers of 80 and 75 wt pct stainless steel composition.[12,13] Another experiment by Zhang[14] prints several layers at 50 wt pct SS316L, skipping over the range which is most susceptible to cracking according to our observations. Hence the FGM literature for Inconel on stainless steel is inconsistent with respect to the observation of cracking at high stainless steel content.

Feenstra *et al.* use direct bonding by depositing 100 wt pct SS316L powder on an IN625 build plate.[15] They do not report cracking. Each point on the lines in Figure 15 represents the stainless steel content of a given single layer. The top row in Figure 15 shows the compositions

of different layers in one of Feenstra's tensile specimens. The second row shows the compositions of different layers of our tensile specimen. The third row shows the compositions of all the single beads and single layers in our experiments, where the shaded region indicates compositions at which the propensity for cracking is high. Feenstra's ultimate tensile strength (UTS) for the specimen, of which two layers are within our shaded region, is 580 MPa and the ductility is 12 pct. Other tensile specimens fabricated by Feenstra contain more layers with compositions with SS316L content in our shaded region. Their UTS values are as high as 606 MPa, but their ductility is at most 15 pct. For our bimetallic tensile specimens in Figure 7 the UTS is 680 MPa and the ductility is 45 pct. The small differences in alloy content between SS316 and SS304 is unlikely to be the source of this significant difference. Although Feenstra does not report cracking, the evidence indicates that high stainless steel content reduces UTS and elongation.

In summary, comparison with literature data indicates that low wt pct SS in the transition regions is beneficial for minimizing defects and maximizing strength of the IN to SS bond.

D. *Welding Literature Comparison*

The welding literature reports some of the same phenomena in the presence of cracking,[42,43] as we observe. Patterson and Milewski use quantitative
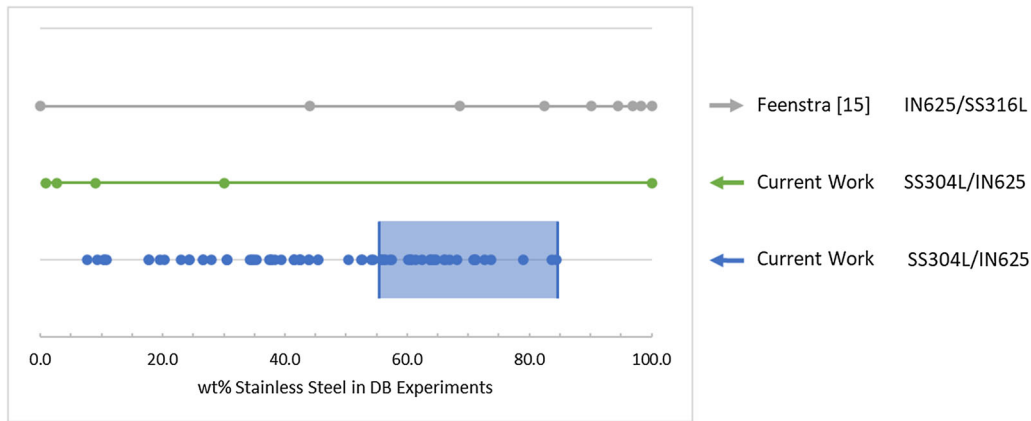
Fig. 15—Weight percent stainless steel in each layer (represented by dots) of directly bonded structures, including single layer builds with a shaded region indicating where cracking is observed. Horizontal arrows indicate that depositions proceed with decreasing SS content except for Feenstra.

Varestraint testing of IN625 welded to SS 304L to determine that crack susceptibility increases monotonically with wt pct SS 304L up to 65 pct, in good agreement with our results. Dupont *et al.* suggest that high sulfur and phosphorous contents, above 0.010 wt pct and 0.020 wt pct respectively, could lead to increased crack susceptibility.[43] This aligns with the experimental results in this work. Our SS304L has a P level of 0.031 wt pct, and as we increase the SS304L in the melt pool we observe cracking when the nominal P content is ~ 0.020 wt pct P. Feenstra's wt pct S and P are not reported. Other welding experiments also observed increased S and P levels around crack surfaces.[44,45] Although solidification cracking with high Nb and Mo segregants between grains appears to be associated with our observations of cracking, the amount of P could play a further detrimental role.

V. CONCLUSIONS

The DED-LB literature is inconsistent with respect to the observation of cracking in the SS304L/IN625 interface. In this work, we consistently find cracking can be avoided in SS304L/IN625 bonds in DED-LB by introducing $\leq$ 50 wt pct SS304L in the interface layers. When cracks are present in an interface layer, they consistently extend into subsequent layers. Hence, they cannot easily be healed. When cracks are absent in the interface layer, the interface survives the thermal cycling induced by the HAZ of subsequent layers. Tensile testing indicates that such interfaces are stronger than the SS304L section of the specimen. Cracking has little dependence on laser power and scan speed, further demonstrating that the wt pct SS304L is the main influence on solidification cracking.

When it occurs, the cracking can be characterized as solidification cracking. The Kou criterion has been designed to compare relative solidification crack susceptibility of similar alloys. However, it is not effective in predicting crack susceptibility of the IN625/SS304L metal mixtures. Similarly, the Modified Kou criterion has poor agreement with the experimental data in this work. Welding literature suggests reducing the amount of S and P by as much as possible can reduce crack susceptibility. It would be valuable in future work to use a lower P content SS304L build plate to see if cracking is reduced.

CONFLICT OF INTEREST

On behalf of all authors, the corresponding author states that there is no conflict of interest.

REFERENCES

1. Y. Miyamoto, W.A. Kaysser, B.H. Rabin, A. Kawasaki, and R.G. Ford, eds.: *Functionally Graded Materials*, vol. 5, Springer, Boston, 1999.
2. A. Reichardt, A.A. Shapiro, R. Otis, R.P. Dillon, J.P. Borgonia, B.W. McEnerney, P. Hosemann, and A.M. Beese: *Int. Mater. Rev.*, 2021, vol. 66, pp. 1–29.
3. P. Kah, M. Shrestha, and J. Martikainen: *Appl. Mech. Mater.*, 2013, vol. 440, pp. 269–76.
4. L.D. Bobbio, R.A. Otis, J.P. Borgonia, R.P. Dillon, A.A. Shapiro, Z.-K. Liu, and A.M. Beese: *Acta Mater.*, 2017, vol. 127, pp. 133–42.
5. L.D. Bobbio, B. Bocklund, A. Reichardt, R. Otis, J.P. Borgonia, R.P. Dillon, A.A. Shapiro, B.W. McEnerney, P. Hosemann, Z.-K. Liu, and A.M. Beese: *J. Alloys Compd.*, 2020, vol. 814, p. 151729.
6. B. Onuike and A. Bandyopadhyay: *Addit. Manuf.*, 2018, vol. 22, pp. 844–51.
7. V.E. Beal, P. Erasenthiran, N. Hopkinson, P. Dickens, and C.H. Ahrens: *J. Mater. Process. Technol.*, 2006, vol. 174, pp. 145–54.
8. I. Shishkovsky, F. Missemer, and I. Smurov: *Phys. Procedia*, 2012, vol. 39, pp. 382–91.
9. M.S. Domack and J.M. Baughman: *Rapid Prototyp. J.*, 2005, vol. 11, pp. 41–51.
10. F.F. Noecker II and J.N. DuPont. DOI:https://doi.org/10.26153/TSW/3840.
11. B.E. Carroll, R.A. Otis, J.P. Borgonia, J. Suh, R.P. Dillon, A.A. Shapiro, D.C. Hofmann, Z.-K. Liu, and A.M. Beese: *Acta Mater.*, 2016, vol. 108, pp. 46–54.
12. B. Chen, Y. Su, Z. Xie, C. Tan, and J. Feng: *Opt. Laser Technol.*, 2020, vol. 123, p. 105916.
13. K. Shah, I. Ul Haq, A. Khan, S.A. Shah, M. Khan, and A.J. Pinkerton: *Mater. Des. 1980–2015*, 2014, vol. 54, pp. 531–38.
14. X. Zhang, Y. Chen, and F. Liou: *Sci. Technol. Weld. Join.*, 2019, vol. 24, pp. 504–16.
15. D.R. Feenstra, A. Molotnikov, and N. Birbilis: *J. Mater. Sci.*, 2020, vol. 55, pp. 13314–3328.
16. N.F. Jones, J.L. Beuth, and M.P. de Boer: *J. Mater. Res.*, 2021, vol. 36, pp. 3701–712.
17. S. Kou: *Acta Mater.*, 2015, vol. 88, pp. 366–74.
18. T. Soysal and S. Kou: *Acta Mater.*, 2018, vol. 143, pp. 181–97.
19. C. Xia and S. Kou: *Sci. Technol. Weld. Join.*, 2020, vol. 25, pp. 690–97.
20. T. Soysal: *Weld. World*, 2021, vol. 65, pp. 1943–954.
21. T. Soysal and B. Erk: *J. Mater. Eng. Perform.*, 2022, https://doi.org/10.1007/s11665-022-07667-7.
22. G. Tang, B.J. Gould, A. Ngowe, and A.D. Rollett: *Metall. Mater. Trans. A*, 2022, vol. 53, pp. 1486–498.
23. K. Zhang, W. Liu, and X. Shang: *Opt. Laser Technol.*, 2007, vol. 39, pp. 549–57.
24. A.B. Spierings, M. Schneider, and R. Eggenberger: *Rapid Prototyp. J.*, 2011, vol. 17, pp. 380–86.
25. S.L. Jeng, H.T. Lee, T.E. Weirich, and W.P. Rebach: *Mater. Trans.*, 2007, vol. 48, pp. 481–89.
26. H. Naffakh, M. Shamanian, and F. Ashrafizadeh: *J. Mater. Process. Technol.*, 2009, vol. 209, pp. 3628–639.
27. S.J. Wolff, S. Lin, E.J. Faierson, W.K. Liu, G.J. Wagner, and J. Cao: *Acta Mater.*, 2017, vol. 132, pp. 106–17.
28. D.F. Susan, J.D. Puskar, J.A. Brooks, and C.V. Robino: *Mater Charact*, 2006, vol. 57, pp. 36–43.
29. Y. Hu, X. Lin, Y. Li, S. Zhang, Q. Zhang, W. Chen, W. Li, and W. Huang: *Mater. Sci. Eng. A*, 2021, vol. 817, p. 141309.
30. M. Rombouts, G. Maes, and R. Persoons: in *Proceedings of the 5th International Conference on Advanced Research in Virtual and Rapid Prototyping*, Taylor & Francis Group, Leiria, 2011, pp. 333–37.
31. M. Rombouts, G. Maes, M. Mertens, and W. Hendrix: *J. Laser Appl.*, 2012, vol. 24, p. 052007.
32. Z. Wang, T.A. Palmer, and A.M. Beese: *Acta Mater.*, 2016, vol. 110, pp. 226–35.
33. Y. Hu, X. Lin, Y. Li, Y. Ou, X. Gao, Q. Zhang, W. Li, and W. Huang: *J. Alloys Compd.*, 2021, vol. 870, p. 159426.
34. G.P. Dinda, A.K. Dasgupta, and J. Mazumder: *Mater. Sci. Eng. A*, 2009, vol. 509, pp. 98–104.
35. L. Qin, C. Chen, M. Zhang, K. Yan, G. Cheng, H. Jing, and X. Wang: *Rapid Prototyp. J.*, 2017, vol. 23, pp. 1119–29.
36. S. Misra, I. Mohanty, M.S. Raza, R. Chakraborty, P. Chatterjee, M. Gopal, S. Ponkshe, P. Saha, and C.S. Kumar: *Surf. Coat. Technol.*, 2022, vol. 447, p. 128818.
37. S. Floreen, G. Fuchs, and W. Yang: in *Superalloys 718, 625, 706 and Various Derivatives*, E.A. Loria, ed., The Minerals, Metals and Materials Society: Pittsburgh, 1994, pp. 13–37.
38. Pandat—Phase Diagram Calculation software package for Multicomponent Systems, Computherm LLC, Middleton, 2001.
39. Thermo-Calc: *Thermo-Calc Software AB*, Stockholm, Sweden, 2021, p. 2021.
40. M. De Oliveira, A. Couto, G. Almeida, D. Reis, N. De Lima, and R. Baldan: *Metals*, 2019, vol. 9, p. 301.
41. G. Barragan, D.A. Rojas Perilla, J. Grass Nuñez, F. Mariani, and R. Coelho: *J. Mater. Eng. Perform.*, 2021, vol. 30, pp. 5297–5306.
42. M.J. Cieslak: *Weld. J.*, 1991, vol. 70, pp. 49s–56s.
43. J.N. DuPont, J.C. Lippold, and S.D. Kiser: *in Welding metallurgy and weldability of nickel-base alloys*, Wiley, Hoboken, 2009, pp. 327–78.
44. R.A. Patterson and J.O. Milewski: *Weld. J.*, 1985, vol. 64, pp. 227s–s231.
45. M. Shakil, M. Ahmad, N.H. Tariq, B.A. Hasan, J.I. Akhter, E. Ahmed, M. Mehmood, M.A. Choudhry, and M. Iqbal: *Vacuum*, 2014, vol. 110, pp. 121–26.